Available online at www.sciencedirect.com
ScienceDirect
Trans. Nonferrous Met. Soc. China 29(2019) 2523−2533
Transactions of Nonferrous Metals Society of China
www.tnmsc.cn

Corrosion behaviour of PEEK or β-TCP-impregnated Ti6Al4V SLM structures targeting biomedical applications

M. M. COSTA[1], T. A. DANTAS[1,2], F. BARTOLOMEU[1], N. ALVES[3], F. S. SILVA[1], G. MIRANDA[1], F. TOPTAN[1,4]

1. Center for Micro Electro Mechanical Systems (CMEMS), University of Minho (UMinho), 4800-058 Guimarães, Portugal;
2. MIT Portugal Program, School of Engineering, University of Minho, Guimarães, Portugal;
3. Centre for Rapid and Sustainable Product Development Polytechnic Institute of Leiria, Rua General Norton de Matos, Apartado 4133, Leiria, Portugal;
4. IBTN/Br – Brazilian Branch of the Institute of Biomaterials, Tribocorrosion and Nanomedicine, UNESP, Campus de Bauru, Av. Eng. Luiz Edmundo Carrijo Coube, 14-01, 17033-360, Bauru, SP, Brazil

Received 29 March 2019; accepted 28 August 2019

Abstract: Ti6Al4V cellular structures were produced by selective laser melting (SLM) and then filled either with beta-tricalcium phosphate (β-TCP) or PEEK (poly-ether-ether-ketone) through powder metallurgy techniques, to improve osteoconductivity and wear resistance. The corrosion behavior of these structures was explored considering its importance for the long-term performance of implants. Results revealed that the incorporation of open cellular pores induced higher electrochemical kinetics when being compared with dense structures. The impregnation of β-TCP and PEEK led to the creation of voids or gaps between the metallic matrix and the impregnated material which also influenced the corrosion behavior of the cellular structures.

Key words: Ti6Al4V cellular structures; corrosion; multimaterial design; poly-ether-ether-ketone (PEEK); beta-tricalcium phosphate (β-TCP)

1 Introduction

Ti6Al4V is one of the most used Ti alloys in biomedical applications, such as orthopedic implants, due to its good mechanical properties. It is a lightweight metal, having high strength, good fracture toughness, low thermal expansion and lower elastic modulus (among metallic biomaterials) [1,2]. Additionally, it presents high biocompatibility and excellent capacity to resist corrosion, associated with the formation of a stable and compact oxide layer on its surface that is created spontaneously when exposed to oxygenated environments [3−6]. However, as other Ti alloys, this material presents no bioactivity which is required to reduce implant-tissue osseointegration time and, subsequently, to promote shorter healing time. Hence, several functionalization techniques are being studied to improve bioactivity [7]. Beta-tricalcium phosphate (β-TCP, $Ca_3(PO_4)_2$), a bioactive material highly similar to the mineral phase of bone, has been applied to overcoming the lack of bioactivity [8−10]. The addition of this ceramic to a Ti matrix is expected to induce a natural bone tissue growth, and consequently promote a faster bone-tissue osseointegration [11,12]. On the other hand, Ti6Al4V also presents poor wear resistance and tends to release metallic ions and wear debris to the surrounding medium [13–15]. To overcome these issues, Poly-ether-ether-ketone (PEEK) and PEEK-based materials have been applied due to their excellent thermal and chemical stability and higher wear resistance, comparing to Ti and its alloys [16,17]. Furthermore, PEEK has excellent mechanical properties, such as low elastic modulus and relatively low manufacturing cost [18].

Selective laser melting (SLM) is an additive manufacturing technique that allows the production of customized and complex 3D parts from CAD data by using laser energy to melt metallic powders in a layer-by-layer process [19−23]. Among all the advantages, the

Corresponding author: T. A. DANTAS; E-mail: telmalvesdantas@gmail.com
DOI: 10.1016/S1003-6326(19)65160-5

SLM technique allows the production of parts without the need for using additional steps [24,25]. Briefly, in this process, 3D CAD data are imported to an SLM software that slices the part into successive layers with a given layer thickness. The metallic powder is spread across the SLM platform and a laser beam scans the powder in predefined sites to melt it and, layer-by-layer, to produce the desired 3D part [20,22,24,26]. The processing parameters like laser power, scan speed, and scan spacing have a huge impact on the SLM components final properties. Many studies have been made to assess the influence of the processing parameters on the final properties of SLM components, in terms of physical, mechanical and microstructural properties [26−29]. BARTOLOMEU et al [26] have investigated the effect of SLM processing parameters on the final properties of Ti6Al4V samples such as density, hardness and shear strength and reported the optimal parameters for this technology on this material. ZHAO et al [30] produced Ti6Al4V alloy by electron beam melting (EBM) and SLM, compared their corrosion behavior in simulated body fluid and reported good corrosion resistance for the samples produced by EBM and SLM that were regarded by authors as suitable for implantation in vivo. However, some authors reported poorer corrosion resistance for the SLM-produced Ti6Al4V alloy due to a large amount of acicular α' and less β-Ti phase in the microstructure [31,32].

Many studies have been made on the production of porous structures, by SLM, to promote bone growth towards the implant, ensuring a good mechanical interlocking between implant and bone [33–35]. However, since these structures will be surrounded by corrosive body fluids, it is essential to assess their corrosion performance. Studies performed on highly-porous Ti [36] and Ti alloy [37] structures showed that increased porosity resulted in the formation of a less protective oxide film on the pore surfaces due to difficulties or delays on the electrolyte penetration through the innermost pores.

Targeting biomedical applications, the present study aimed to evaluate the effect of porosity and the incorporation of β-TCP or PEEK on the corrosion behavior of Ti6Al4V-SLM structures. Ti6Al4V cellular structures were designed and produced by SLM in a way to obtain near-net-shape structures according to the predefined CAD model. Using these multifunctional structures, it can be possible to reduce the elastic modulus, to promote the bone ingrowth, as well, to improve the bioactivity and wear resistance by impregnating β-TCP and PEEK, respectively, into the open cells.

2 Experimental

2.1 Starting materials

The Ti6Al4V starting powders used to produce the SLM samples were supplied from SLM solutions (Germany). Table 1 and Fig. 1(a) show the composition and particle size, respectively, according to the manufacturers.

Table 1 Composition of Ti6Al4V powders (wt.%)

Al	V	C	Fe	O	N	H	Ti
6.4	3.8	0.01	0.23	0.12	0.02	0.0074	Bal.

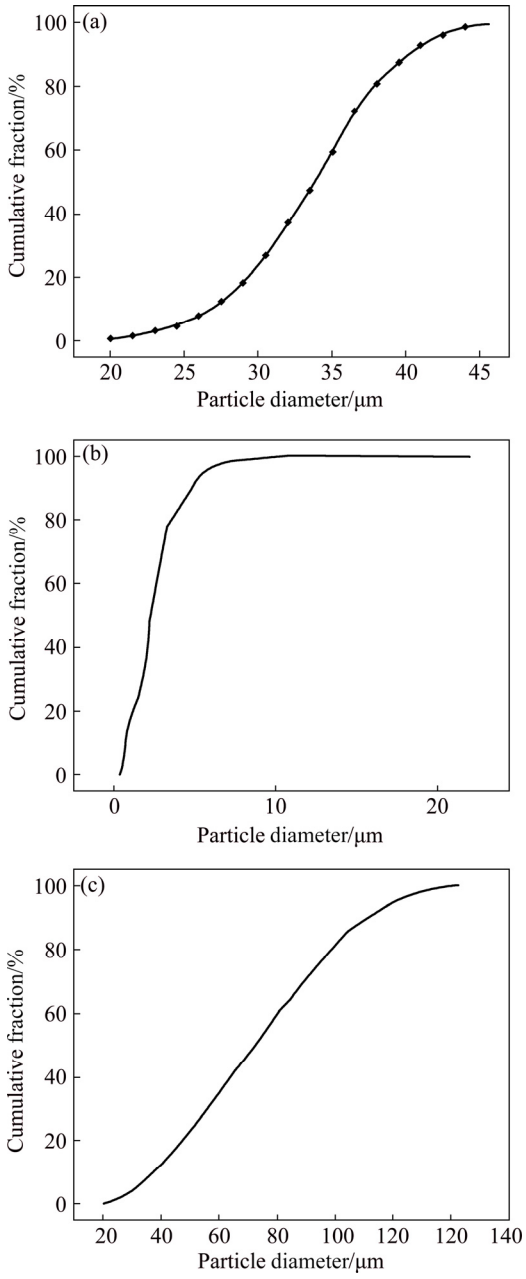

Fig. 1 Powder size distributions of Ti6Al4V (a), β-TCP (b) and PEEK (c)

After producing the Ti6Al4V cellular structures, two approaches were evaluated: bioactive impregnation of β-TCP and polymer impregnation of PEEK. The bioactive impregnation using β-TCP was carried out by using press and sintering technique. β-TCP powder was supplied from Trans-Tech, Inc, with a particle size distribution as presented in Fig. 1(b). The polymer impregnation using PEEK was carried out by using hot pressing. PEEK powder was supplied from Evonik Industries, with the particle size distribution presented in Fig. 1(c).

2.2 Processing

To fabricate dense and cellular structured Ti6Al4V samples, a commercial SLM equipment (SLM solutions, model 125HL) was used. The main characteristics of the equipment are shown in Table 2. Briefly, this equipment has an Yb-faser-laser, a focus beam diameter of 87 μm and a maximum laser power of 100 W. The process occurs under an Ar/N_2 atmosphere keeping the temperature of the building platform at 200 °C. The present study used SLM processing parameters, a laser power of 90 W, a scan speed of 600 mm/s, a scan spacing of 80 μm and a layer thickness of 30 μm.

Four different types of Ti6Al4V or Ti6Al4V-based samples were produced and investigated. Table 3 gives the component type and processing technique for each group of samples.

After producing the cellular structured parts (SP2), β-TCP (SP3) and PEEK (SP4) were introduced into the available open cells (Fig. 2). On SP3 samples, β-TCP impregnation was performed through a press and sintering process. In this process, the cellular structures were placed in a steel mold. Thereafter, a solution of

Table 2 SLM equipment (model 125 HL) characteristics

Laser type	Effective build volume/ mm^3	Laser power/ W	Scanning speed/ $(mm\cdot s^{-1})$	Layer thickness/ μm	Distance between scanning lines/mm	Laser spot/ μm	Inert gas (Ar/N_2) flow during production/ $(L\cdot min^{-1})$	Inert gas (Ar/N_2) flow during filling of chamber/$(L\cdot min^{-1})$
Yb-faser-laser	125×125×125	40−100	100−2000	20−40	0.07−0.15	87	0.5	10

Table 3 Testing samples

Sample No.	Ti6Al4V component type	Processing technique
SP1	Dense structure	SLM
SP2	Cellular structure	SLM
SP3	Cellular structure impregnated with β-TCP	SLM + press and sintering
SP4	Cellular structure impregnated with PEEK	SLM + hot pressing

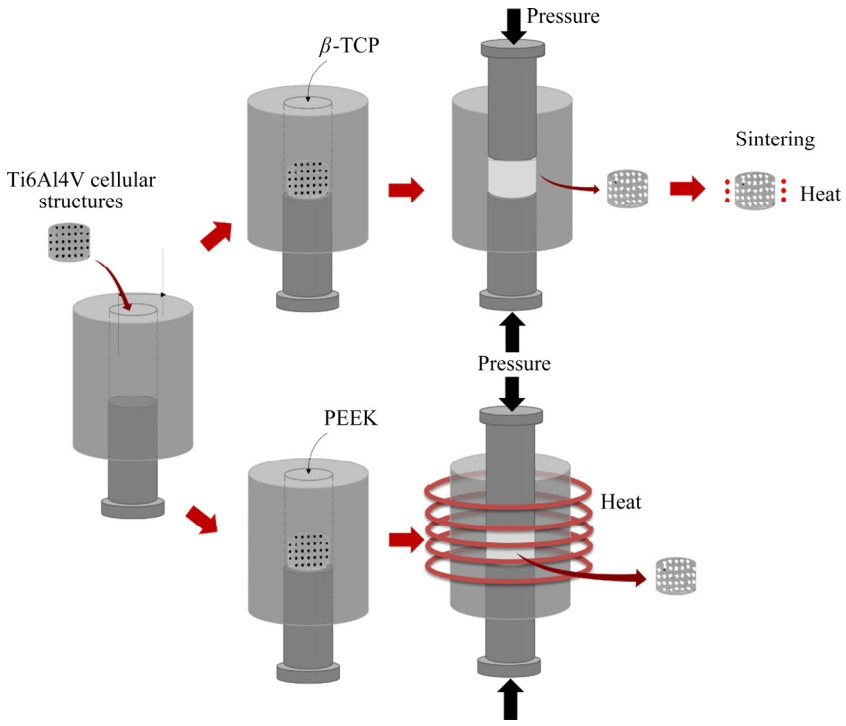

Fig. 2 Fabrication details of Ti6Al4V cellular structures impregnated with β-TCP or PEEK

β-TCP powder and acetone was prepared and introduced into a steel mold where the cellular structure was already properly positioned. Then, using an upper punch, the pressure was slowly applied by a hydraulic press to force this solution to occupy the open cells. After 10 min under pressure, the samples were removed from the mold. To sinter the β-TCP powders, a subsequent sintering step was performed in a tubular furnace at 1100 °C for 2 h under a high vacuum (10^{-3} Pa), with heating and cooling rates of 5 °C/min.

On SP4 samples, hot pressing was used to impregnate PEEK by applying simultaneously pressure and temperature. The cellular structures were inserted inside a steel mold, followed by the introduction of PEEK powder. After placing and positioning the mold inside the chamber, a residual pressure was applied to compressing the powder. Posteriorly, the mold was heated until 380 °C (above PEEK melting point of 345 °C). Finally, the induction heating was turned off to decrease the temperature down to 300 °C and PEEK was pressed under 25 MPa for 5 s, to force it to fill the available space inside the open cells.

2.3 Microstructural analysis

Field emission gun scanning electron microscopy (FEG SEM, FEI Nova 200, USA) was used to characterize the surfaces before and after testing. The effect of the impregnation method on the microstructure of Ti6Al4V was evaluated on the surfaces etched with Kroll's reagent (5% HNO_3, 10% HF and 85% distilled water) and analyzed by SEM. Before corrosion tests, crystalline structures were characterized with X-ray diffraction using Bruker AXS D8 Discover equipment. Diffraction data were collected from 10° to 80° of 2θ, with a step size of 0.02° and counting time of 1 s/step.

2.4 Corrosion tests

Before testing, all samples were polished with different abrasive silicon carbide papers, ranging from 0.125 to 0.0374 mm grit size. After grinding, samples were ultrasonically cleaned with propanol for 30 min in the case of SP2 and 10 min in the other three conditions. Regarding the cellular structure (SP2), due to its complex geometry, cleaning was done in a net positioned upside down, to avoid the accumulation of debris coming from grinding.

A three-electrode cell assembly comprising the sample as the working electrode, a platinum electrode as the counter electrode, a saturated calomel electrode as the reference electrode, and 40 mL of NaCl (9 g/L) solution as the electrolyte was used for the electrochemical tests. Open-circuit potential (OCP) and cyclic polarization were carried out using a Gamry Potentiostat/Galvanostat/ZRA (Reference 600) equipment on samples having a geometric exposed area of 0.36 cm^2 that was also used for normalizing the electrochemical results for SP1 samples. The exposed areas of SP2 and SP3 were calculated from the CAD model whereas only the metallic exposed area was considered for SP4 samples. Before cyclic polarization, OCP values were monitored until stabilization (the values of potential did not vary more than 40 mV in 1 h). Cyclic polarization curves were acquired using a scan rate of 1 mV/s, starting at −0.2 V (vs OCP), and the sweep direction was reversed at 1 V (vs SCE).

3 Results and discussion

3.1 Microstructural characterization

Figure 3 shows the representative morphologies of the raw powders. Figures 3(a), (b) and (c) correspond to

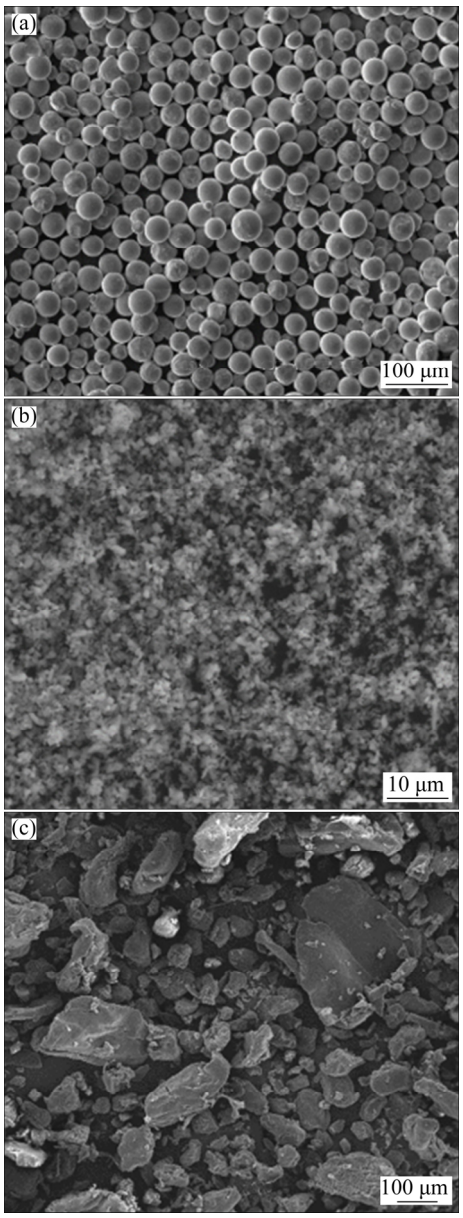

Fig. 3 SEM images of raw powders: (a) Ti6Al4V; (b) β-TCP; (c) PEEK

the Ti6Al4V, β-TCP and PEEK powders, respectively. From these figures, it is possible to observe that Ti6Al4V had a spherical shape, β-TCP powder was characterized by an aggregate of spherical particles and PEEK powder had an irregular shape.

3D parts, produced by SLM based on the CAD data, are presented in Fig. 4. It is possible to verify from the images that the samples were successfully produced by this technique, once the geometry of the CAD model and the SLM processed sample was very similar.

Figure 5 presents the samples before corrosion testing. Regarding SP1 (dense) samples (Fig. 5(a)), no evidence of pronounced porosity was observed, suggesting that the processing technique was efficient to promote the densification of the samples. The open cellular structures can be seen in Fig. 5(b) showing the viability of SLM to produce such geometries. On the other hand, Figs. 5(c) and (d) show the Ti6Al4V cellular structures impregnated with β-TCP and PEEK, respectively. It was possible to observe that the impregnation process of β-TCP was not as efficient as PEEK, once the holes were not totally filled with the ceramic material.

Figure 6 presents the XRD patterns of each sample. Regarding SP1 and SP2 samples, no significant differences were detected in the XRD pattern where hexagonal close-packed (HCP) and body-centered cubic (BCC) crystalline structures of Ti were detected. On the other hand, by adding β-TCP to the cellular structure (SP3), it was possible to observe a new peak (≈31°) that corresponds to the β-TCP phase. Analyzing the SP4 pattern, new peaks were observed corresponding to the PEEK pattern, which is in accordance with the XRD patterns for this material [38−40].

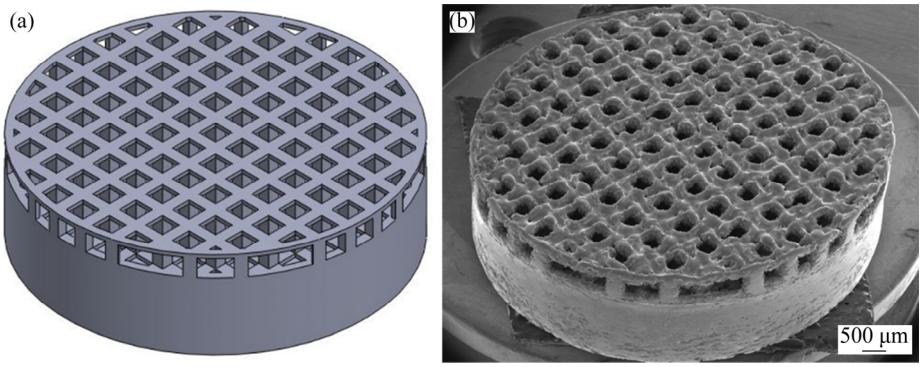

Fig. 4 SLM structure of CAD model (a) and as-built sample (b)

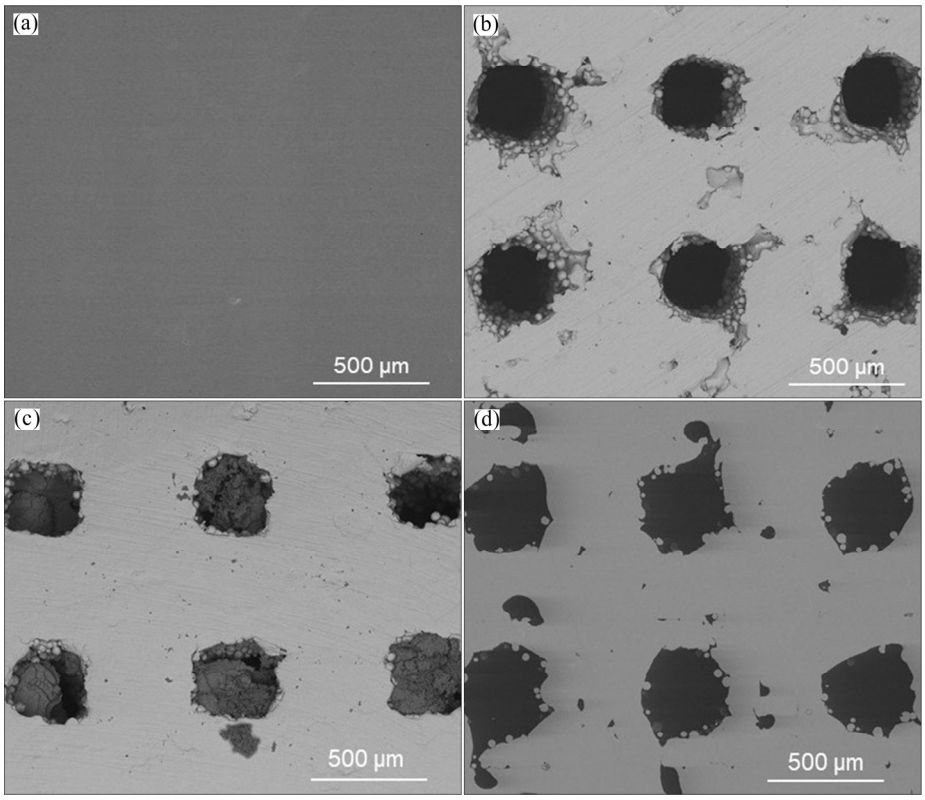

Fig. 5 SEM images of SLM-produced samples: (a) SP1; (b) SP2; (c) SP3; (d) SP4

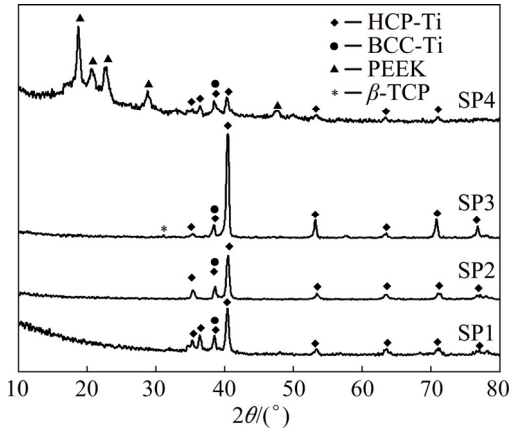

Fig. 6 XRD patterns of tested samples showing distinctive phase constituents

The acid etched microstructures of the metallic matrix of SP1, SP2, SP3, and SP4 are given in Fig. 7. Ti6Al4V alloy is known for its structure composed of α phase (HCP) and β phase (BCC). SEM images revealed the presence of acicular α' martensite, that is hard to observe on the XRD spectra since α and α' phases have HCP structure with very close lattice parameters [32]. The XRD results of SP3 together with the microstructure presented in Fig. 7(c) suggested that the martensite phase was decomposed into α and β phases when subjected to high temperatures (temperatures above the β transus) [41].

3.2 Corrosion behavior

In order to normalize the electrochemical data, the electrolyte exposed area of 1.92 cm^2 for the SP2 calculated from the CAD model by considering the following areas is shown in Fig. 8, where A_1 is the area of the pore walls (green) that are presented both on top and bottom of the sample, A_2 corresponds to the area of the interconnecting walls between pores, A_3 represents the superficial area (blue) of the sample, A_4 is the bottom area (orange) and A_5 represents the top walls (red).

As it is shown in Fig. 5(c), the β-TCP impregnation was not fully achieved on SP3. In this sense, the exposed area was determined on the CAD model (Fig. 9) by considering the areas shown by arrows in Fig. 9 (top areas of A_1, A_2, A_3, and A_5). According to this assumption, the exposed area is calculated as 1.23 cm^2. Nevertheless, it is worthy to stress that these area calculations are approximations and particularly on SP3, the irregularity inside the open cells made it difficult to obtain accurate calculations. Therefore, future works on the optimized samples should use more accurate techniques, such as micro-CT, to calculate the exposed area more precisely. For the SP4 sample, since the impregnation was almost fully achieved, only the metallic area was considered (0.26 cm^2).

The cyclic polarization curves of the different tested materials are presented in Fig. 10. Average values of the last 10 minutes of φ_{OCP}, corrosion potential ($\varphi_{(i=0)}$) and corrosion current density (J_{corr}) (obtained by Tafel extrapolation), and J_{pass} values (derived from the curves) are given in Table 4. As it is very well known [3,42], Ti has a strong affinity to oxygen which leads to its ability to create a stable passive film in any environment that contains oxygen, characterized by a well-defined passivation plateau. The reverse curves of all tested materials evolved on the left-hand side of the forward

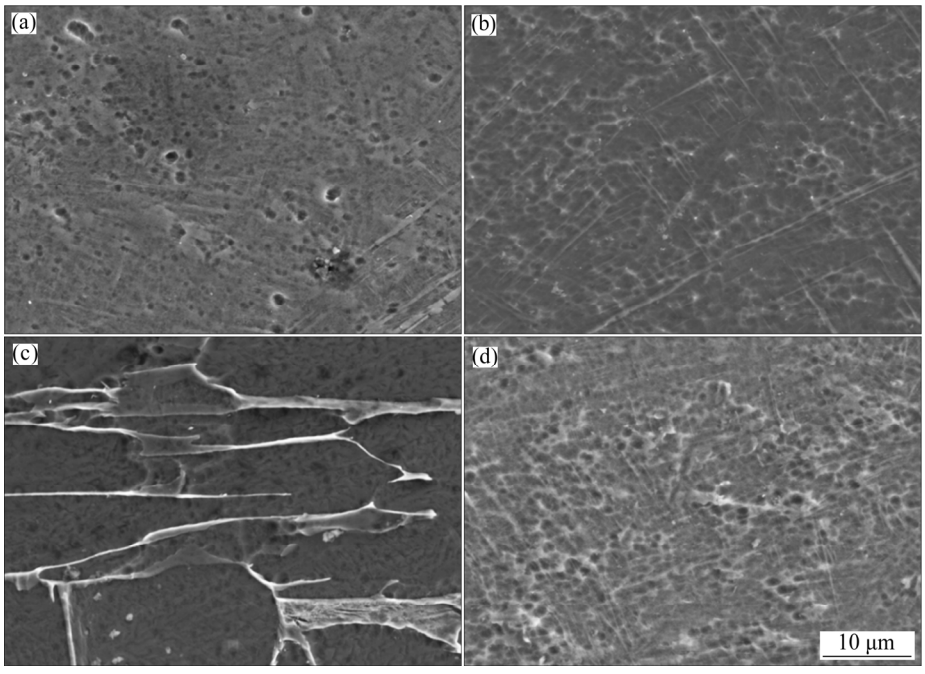

Fig. 7 SEM images of acid etched samples: (a) SP1; (b) SP2; (c) SP3; (d) SP4

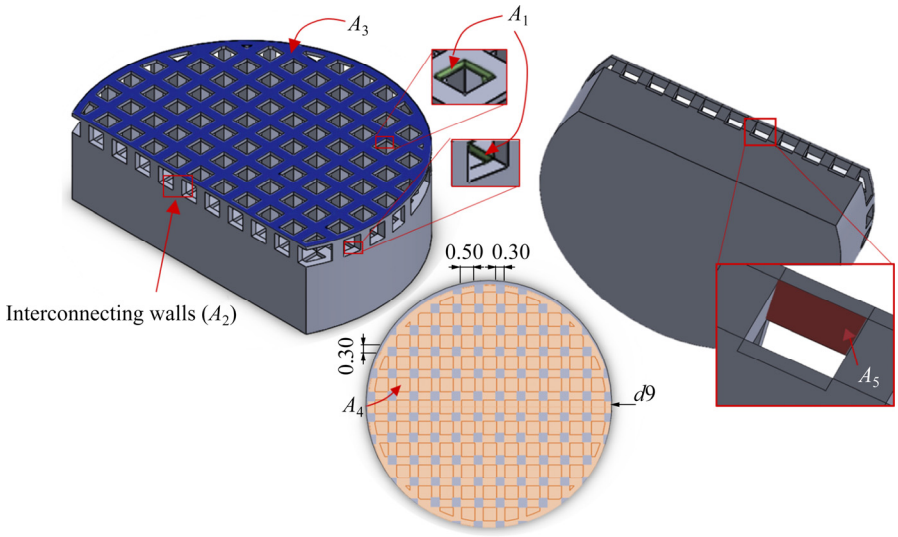

Fig. 8 Schematic representation of total area in contact with electrolyte for cellular structures (unit: mm)

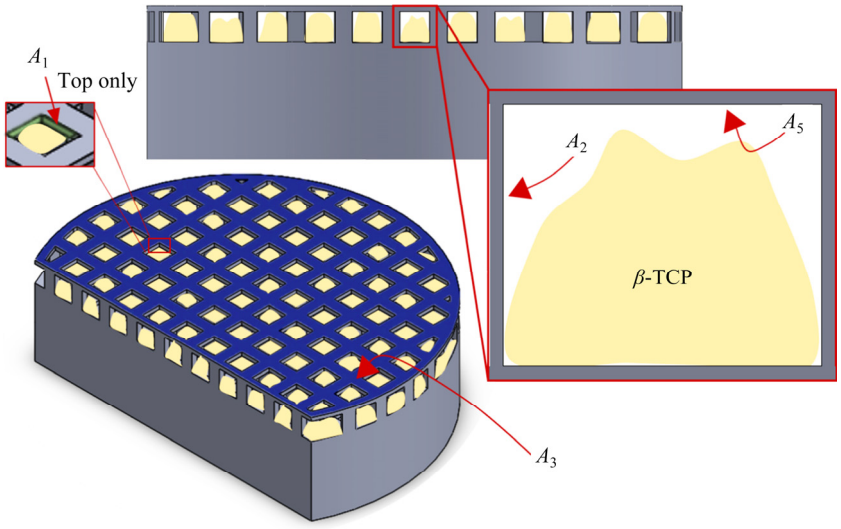

Fig. 9 Schematic representation of total area in contact with electrolyte for SP3 sample

curves, i.e., for the same potential the current density on the backward scan presented lower values, indicating their ability to resist to localized corrosion [43].

A clear passivation plateau was observed on the cyclic polarization curve of SP1 (Fig. 10(a)) at $(0.39\pm0.04)\times10^{-5}$ A/cm^2 (J_{pass}). On the other hand, the transition from cathodic to anodic domain was characterized by a $\varphi_{(i=0)}$ of (−423±25) mV (Table 4). The representative evaluation of the cyclic polarization curve of the cellular structures (SP2) is presented in Fig. 10(b). The forward scan was characterized by a $\varphi_{(i=0)}$ of (−141±59) mV (Table 4) with a passivation current density (J_{pass}) of $(1.53\pm0.07)\times10^{-5}$ A/cm^2. The passivation plateau observed on SP2 shifted to higher current density values and presented some local increments on the current. These samples were characterized by the existence of interconnected holes that may allow a delay in electrolyte flow, that eventually may result in creation of less protective oxide film on the inner cell surface, which may be responsible for the increased J_{pass} values, as already reported for Ti [36] and Ti−Nb based [37] highly-porous structures. Nevertheless, since the exposed area was calculated over a CAD model, and since as-built samples presented rough cell surfaces (Fig. 5), the real exposed area may be increased, which may have an influence on obtaining increased J_{pass} values.

Figure 10(c) represents the cyclic polarization curve of SP3. Despite having lower corrosion potential compared with SP2, $\varphi_{(i=0)}$=(−492±18) mV, it has the capability of forming a stable passive film evidenced by a well-marked passivation plateau. Furthermore, comparing SP1 and SP3 polarization curves, the corrosion potentials of both plots were very similar ($\varphi_{(i=0)}$=(−423±25) mV vs $\varphi_{(i=0)}$=(−492±18) mV). However, J_{pass} of SP3 was higher than that of SP1 ($(2.51\pm0.02)\times10^{-5}$ A/cm^2). As also mentioned above,

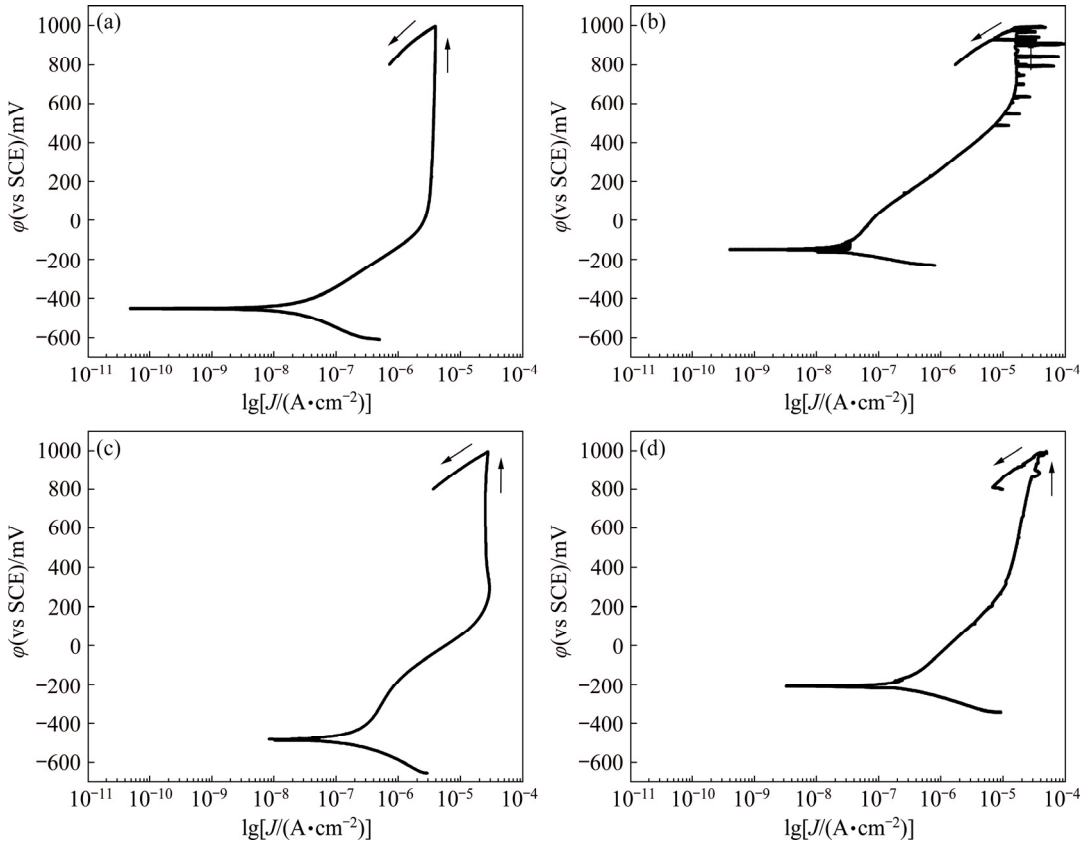

Fig. 10 Cyclic polarization curves of tested materials: (a) SP1; (b) SP2; (c) SP3; (d) SP4

Table 4 Electrochemical data derived from cyclic polarization curves for tested materials

Sample	φ_{OCP}	$\varphi_{(i=0)}$/ mV	J_{corr}/ (10^{-7} A·cm^{-2})	J_{pass}/ (10^{-5} A·cm^{-2})
SP1	−386±23	−423±25	−	0.39±0.04
SP2	−59±53	−141±59	−	1.53±0.07
SP3	−459±22	−492±18	−	2.51±0.02
SP4	−153±10	−209±22	5.03±0.49	−

although a model was followed to calculate the exposed area on SP3 sample, this model may have some deviations since it is very difficult to simulate the impregnation process with β-TCP, that eventually may lead to a deviation on the J_{pass} values, in addition to the possible heterogeneities on the passive film due to the delays on the electrolyte penetration.

Figure 10(d) shows the cyclic polarization curves of samples impregnated with PEEK (SP4). The corrosion potential of this material was (−209±22) mV and J_{corr} was (5.03±0.49)×10^{-7} A/cm^2. It was possible to observe that for these samples that there was a deviation on the passivation plateau, which can be related with the presence of some narrow gaps between the polymeric and metallic transition that might act as active zones that, consequently, promoted some discontinuities on the passive film [44].

Therefore, although the presence of β-TCP and PEEK was not expected to influence directly the corrosion behavior of Ti6Al4V, the impregnation process led to some interfacial voids or gaps between the impregnated material and the metallic matrix that eventually influenced the corrosion behavior of these structures.

Figure 11 shows the SEM micrographs of the surfaces after corrosion testing. There were no visible changes in the surface morphology on none of the samples when compared with the as-processed ones. However, further analysis of the impregnated samples (Figs. 11(c) and (d)) may explain the different results obtained on the electrochemical tests. As already mentioned, and as can be seen in Fig. 11(c), the impregnation process was not fully accomplished on SP3, which led to increased exposed area and possibly led to some difficulties on electrolyte penetration that apparently influenced the corrosion behavior. Moreover, in the case of SP4 (Fig. 11(d)), the impregnation process was fully achieved; however, some gaps were visible on the material surface that apparently affected the corrosion behavior. Therefore, these results showed that further work should be performed to optimize the impregnation process to avoid discontinuities at the interface between the impregnated material and the

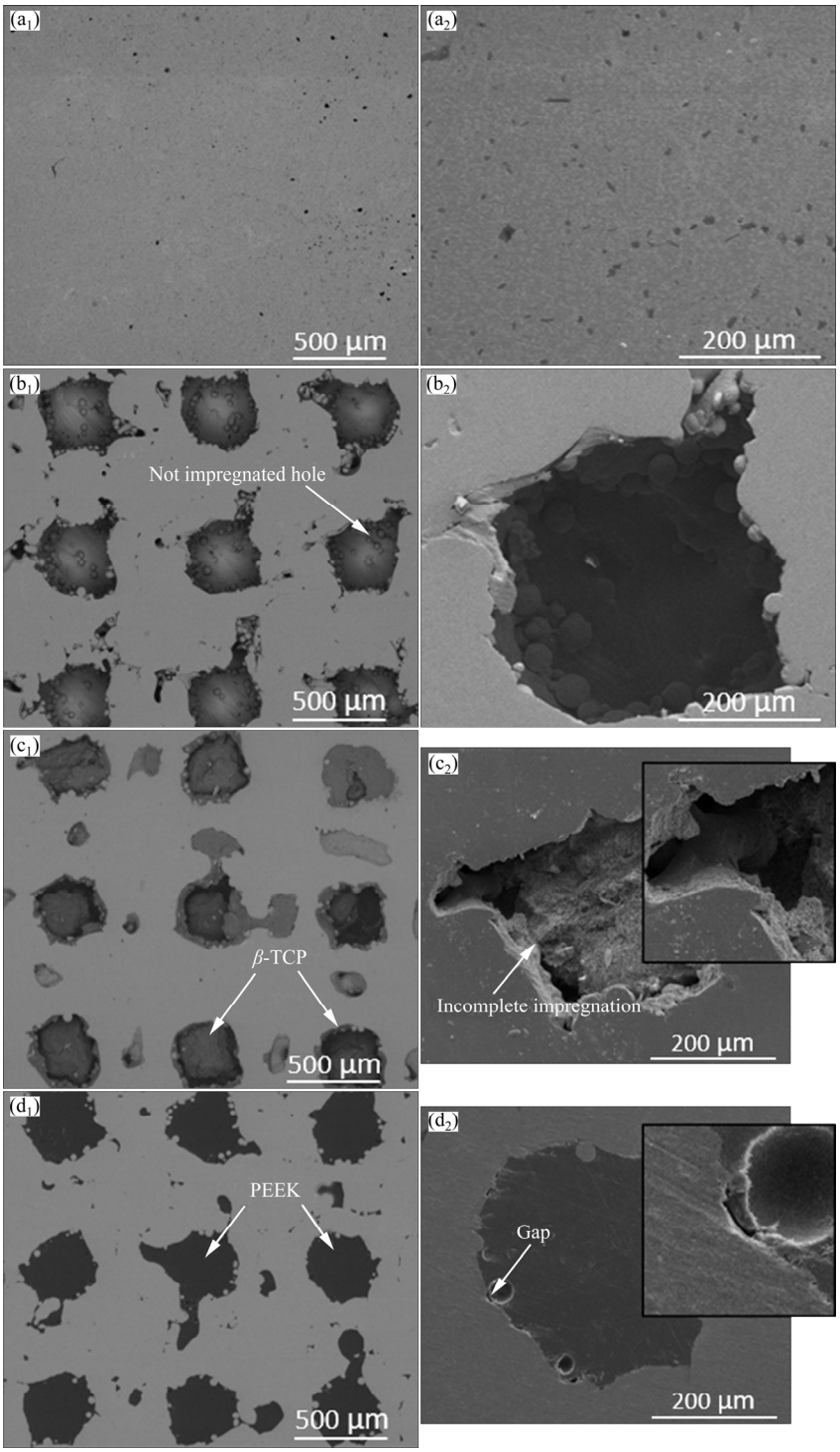

Fig. 11 Lower and higher magnification SEM micrographs of surfaces after corrosion tests: (a) SP1; (b) SP2; (c) SP3; (d) SP4

metallic matrix. After optimization, further electrochemical analysis such as electrochemical impedance spectroscopy should be carried out to better understand the corrosion mechanisms.

4 Conclusions

(1) Processing of Ti6Al4V alloy by SLM led to the formation of acicular α' martensite, along with α and β phases. Further sintering process applied for β-TCP resulted in the decomposition of the martensite phase into α and β phases.

(2) Corrosion studies revealed that the introduction of open cellular porosity on Ti6Al4V or uncompleted impregnation process could influence the corrosion behavior through the presence of interconnected pores or gaps between the metal and the impregnated material leading to the difficulties or delays on the electrolyte

penetration that may create heterogeneities on the passive film.

(3) No evidence of localized corrosion was observed on the polarization curves neither for the cellular structures nor for the β-TCP or PEEK impregnated structures; however, some narrow gaps between the impregnated PEEK and the Ti6Al4V matrix probably acted as active zones and promoted some discontinuities on the passive film.

Acknowledgments

This work was supported by FCT through the grants PD/BD/140202/2018, SFRH/BD/140191/2018 and SFRH/BD/128657/2017, and the projects PTDC/EMS-TEC/5422/2014 and NORTE-01-0145-FEDER-000018-HAMaBICo. Additionally, this work was supported by FCT with the reference project UID/EEA/04436/2019. F. TOPTAN is grateful for the financial support through the M-ERA-NET/0001/2015 project (FCT).

References

[1] NIINOMI M. Biologically and mechanically biocompatible titanium alloys Ti−6Al−4V ELI [J]. Materials Transactions, 2008, 49: 2170−2178.

[2] KAHRAMAN N, GULENC B, FINDIK F. Corrosion and mechanical-microstructural aspects of dissimilar joints of Ti−6Al−4V and Al plates [J]. International Journal of Impact Engineering, 2007, 34: 1423−1432.

[3] LICAUSI M P, IGUAL MUÑOZ A, BORRÁS V A. Tribocorrosion mechanisms of Ti6Al4 V biomedical alloys in artificial saliva with different pHs [J]. Journal of Physics D: Applied Physics, 2013, 46: 404003.

[4] SOUZA J C M, BARBOSA S L, ARIZA E, CELIS J P, ROCHA L A. Simultaneous degradation by corrosion and wear of titanium in artificial saliva containing fluorides [J]. Wear, 2012, 292−293: 82−88.

[5] RATNER B D, HOFFMAN A, SCHOEN F, LEMONS J. Biomaterials science: An introduction to materials in medicine [M]. Third ed. USA: Elsevier, 2013.

[6] COSTA M M, BARTOLOMEU F, ALVES N, SILVA F S, MIRANDA G. Tribological behavior of bioactive multi-material structures targeting orthopedic applications [J]. Journal of the Mechanical Behavior of Biomedical Materials, 2019, 94: 193−200.

[7] YILMAZ E, ÇAKIROĞLU B, GÖKÇE A, FINDIK F, GULSOY H O, GULSOY N, MUTLU Ö, ÖZACAR M. Novel hydroxyapatite/graphene oxide/collagen bioactive composite coating on Ti16Nb alloys by electrodeposition [J]. Materials Science and Engineering C, 2019, 101: 292−305.

[8] OGOSE A, HOTTA T, KAWASHIMA H, KONDO N, GU W, KAMURA T, ENDO N. Comparison of hydroxyapatite and beta tricalcium phosphate as bone substitutes after excision of bone tumors [J]. Journal of Biomedical Materials Research, Part B: Applied Biomaterials, 2004, 72B: 94−101.

[9] DANTAS T A, ABREU C S, COSTA M M, MIRANDA G, SILVA F S, DOURADO N, GOMES J R. Bioactive materials driven primary stability on titanium biocomposites [J]. Materials Science and Engineering C, 2017, 77: 1104−1110.

[10] COSTA M M, LIMA R, MELO-FONSECA F, BARTOLOMEU F, ALVES N, MIRANDA A, GASIK M, SILVA F S, SILVA N A, MIRANDA G. Development of β-TCP−Ti6Al4V structures: Driving cellular response by modulating physical and chemical properties [J]. Materials Science and Engineering C, 2019, 98: 705−716.

[11] ZHANG S, XIANTING Z, YONGSHENG W, KUI C, WENJIAN, W. Adhesion strength of sol–gel derived fluoridated hydroxyapatite coatings [J]. Surface and Coatings Technology, 2006, 200: 6350−6354.

[12] MOHSENI E, ZALNEZHAD E, BUSHROA A R. Comparative investigation on the adhesion of hydroxyapatite coating on Ti−6Al−4V implant : A review paper [J]. International Journal of Adhesion and Adhesives, 2014, 48: 238−257.

[13] CINTIA S, MILANI M. Evaluation of the stress distribution in CFR-PEEK dental implants by the three-dimensional finite element method [J]. Journal of Materials Science: Materials in Medicine, 2010, 21: 2079−2085.

[14] MEENEN N M, LEHMANN W. Response of primary fibroblasts and osteoblasts to plasma treated polyetheretherketone (PEEK) surfaces [J]. Journal of Materials Science: Materials in Medicin, 2005, 6: 671−677.

[15] DANTAS T A, COSTA M M, MIRANDA G, SILVA F S, ABREU C S, GOMES J R. Effect of HAp and β-TCP incorporation on the tribological response of Ti6Al4V biocomposites for implant parts [J]. Journal of Biomedical Materials Research, Part B: Applied Biomaterials, 2018, 106: 1010−1016.

[16] CHEN F, OU H, LU B, LONG H. A constitutive model of polyether-ether-ketone [J]. Journal of the Mechanical Behavior of Biomedical Materials, 2016, 53: 427−433.

[17] ZHOU L, QIAN Y, ZHU Y, LIU H, GAN K, GUO J. The effect of different surface treatments on the bond strength of PEEK composite materials [J]. Dental Materials, 2014, 30: 209−215.

[18] GARCIA-GONZALEZ D, RODRIGUEZ-MILLAN M, RUSINEK A, ARIAS A. Low temperature effect on impact energy absorption capability of PEEK composites [J]. Composite Structures, 2015, 134: 440−449.

[19] TAKEZAWA A, KOBASHI M, KOIZUMI Y, KITAMURA M. Porous metal produced by selective laser melting with effective isotropic thermal conductivity close to the Hashin-Shtrikman bound [J]. International Journal of Heat and Mass Transfer, 2017, 105: 564−572.

[20] SPIERINGS A B, DAWSON K, HEELING T, UGGOWITZER P J, SCHÄUBLIN R, PALM F, WEGENER K. Microstructural features of Sc- and Zr-modified Al−Mg alloys processed by selective laser melting [J]. Materials & Design, 2017, 115: 52−63.

[21] MILTON S, MORANDEAU A, CHALON F, LEROY R. Influence of finish machining on the surface integrity of Ti6Al4V produced by selective laser melting [C]//3rd CIRP Conference on Surface Integrity (CIRP CSI). Charlotte, North Carolina, UAS: Elsevier, 2016: 127−130.

[22] BOSCHETTO A, BOTTINI L, VENIALI F. Roughness modeling of AlSi10Mg parts fabricated by selective laser melting [J]. Journal of Materials Processing Technology, 2017, 241: 154−163.

[23] SUN J, YANG Y, WANG D. Parametric optimization of selective laser melting for forming Ti6Al4V samples by Taguchi method [J]. Optics & Laser Technology, 2013, 49: 118−124.

[24] YADROITSEV I, BERTRAND P, SMUROV I. Parametric analysis of the selective laser melting process [J]. Applied Surface Science, 2007, 253: 8064−8069.

[25] BARTOLOMEU F, BUCIUMEANU M, PINTO E, ALVES N, SILVA F S, CARVALHO O, MIRANDA G. Wear behavior of Ti6Al4V biomedical alloys processed by selective laser melting, hot pressing and conventional casting [J]. Transactions of Nonferrous Metals Society of China, 2017, 27: 829−838.

[26] BARTOLOMEU F, FARIA S, CARVALHO O, PINTO E, ALVES N, SILVA F S, MIRANDA G. Predictive models for physical and mechanical properties of Ti6Al4V produced by selective laser melting [J]. Materials Science and Engineering A, 2016, 663:

181−192.
[27] ZHANG H, ZHU H, QI T, HU Z, ZENG X. Selective laser melting of high strength Al−Cu−Mg alloys: Processing, microstructure and mechanical properties [J]. Materials Science and Engineering A, 2016, 656: 47−54.
[28] HAO L, DADBAKHSH S, SEAMAN O, FELSTEAD M. Selective laser melting of a stainless steel and hydroxyapatite composite for load-bearing implant development [J]. Journal of Materials Processing Technology, 2009, 209: 5793−5801.
[29] BORDIN A, SARTORI S, BRUSCHI S, GHIOTTI A. Experimental investigation on the feasibility of dry and cryogenic machining as sustainable strategies when turning Ti6Al4V produced by Additive Manufacturing [J]. Journal of Cleaner Production, 2017, 142: 4142−4151.
[30] ZHAO B, WANG H, QIAO N, WANG C, HU M. Corrosion resistance characteristics of a Ti-6Al-4V alloy scaffold that is fabricated by electron beam melting and selective laser melting for implantation in vivo [J]. Materials Science and Engineering C, 2017, 70: 832−841.
[31] DAI Nian-wei, ZHANG Lai-chang, ZHANG Jun-xi, CHEN Qi-meng, WU Mao-liang. Corrosion behaviour of selective laser melted Ti−6Al−4V alloy in NaCl solution [J]. Corrosion Science, 2016, 102: 484−489.
[32] TOPTAN F, ALVES A C, CARVALHO O, BARTOLOMEU F, PINTO A M, SILVA F S, MIRANDA G. Corrosion and tribocorrosion behavior of Ti6Al4V produced by selective laser melting and hot pressing in comparison with the commercial alloy [J]. Journal of Materials Processing Technology, 2019, 266: 239−245.
[33] ARABNEJAD S, BURNETT JOHNSTON R, PURA J A, SINGH B, TANZER M, PASINI D. High-strength porous biomaterials for bone replacement: A strategy to assess the interplay between cell morphology, mechanical properties, bone ingrowth and manufacturing constraints [J]. Acta Biomaterialia, 2016, 30: 345−356.
[34] BARTOLOMEU F, SAMPAIO M, CARVALHO O, PINTO E, ALVES N, GOMES J R, SILVA F S, MIRANDA G. Tribological behavior of Ti6Al4V cellular structures produced by Selective Laser Melting [J]. Journal of the Mechanical Behavior of Biomedical Materials, 2017, 69: 128−134.
[35] TANIGUCHI N, FUJIBAYASHI S, TAKEMOTO M, SASAKI K, OTSUKI B, NAKAMURA T, MATSUSHITA T, KOKUBO T, MATSUDA S. Effect of pore size on bone ingrowth into porous titanium implants fabricated by additive manufacturing: An in vivo experiment [J]. Materials Science and Engineering C, 2016, 59: 690−701.
[36] ALVES A, ARIZA E, TOPTAN F, PONTHIAUX P, PINTO A M. Corrosion behaviour of porous Ti intended for biomedical applications [J]. Journal of Porous Materials, 2016, 23: 1261−1268.
[37] YILMAZ E, GÖKÇE A, FINDIK F, GULSOY H O, İYIBILGIN O. Mechanical properties and electrochemical behavior of porous Ti−Nb biomaterials [J]. Journal of the Mechanical Behavior of Biomedical Materials, 2018, 87: 59−67.
[38] WANG N, YANG Z, THUMMAVICHAI K, XU F, HU C, CHEN H, XIA Y, ZHU Y. Novel graphitic carbon coated IF-WS 2 reinforced poly(ether ether ketone) nanocomposites [J]. Royal Society of Chemistry Advances, 2017, 7: 35265−35273.
[39] DÍEZ-PASCUAL A M, XU C, LUQUE R. Development and characterization of novel poly(ether ether ketone)/ZnO bionanocomposites [J]. Journal of Materials Chemistry B, 2014, 2: 3065−3078.
[40] HAN C M, LEE E J, KIM H E, KOH Y H, KIM K N, HA Y, KUH S U. The electron beam deposition of titanium on polyetheretherketone (PEEK) and the resulting enhanced biological properties [J]. Biomaterials, 2010, 31: 3465−3470.
[41] VRANCKEN B, THIJS L, KRUTH J P, VAN HUMBEECK J. Heat treatment of Ti6Al4V produced by selective laser melting: Microstructure and mechanical properties [J] Journal of Alloys and Compounds, 2012, 541: 177−185.
[42] JACKSON M J, AHMED W. Surface engineered surgical tools and medical devices [M]. USA: Springer, 2007.
[43] BHOLA R, BHOLA S M, MISHRA B, OLSON D L. Electrochemical behavior of titanium and its alloys as dental implants in normal saline [J]. Research Letters in Physical Chemistry, 2009, 2009: 1−4.
[44] RIBEIRO A M, ALVES A C, SILVA F S, TOPTAN F. Electrochemical characterization of hot pressed CoCrMo-HAP biocomposite in a physiological solution [J]. Materials and Corrosion, 2015, 66: 790−795.

PEEK 或 β-TCP 充填的生物医用 Ti6Al4V 激光选区熔化结构的腐蚀行为

M. M. COSTA[1], T. A. DANTAS[1,2], F. BARTOLOMEU[1], N. ALVES[3], F. S. SILVA[1], G. MIRANDA[1], F. TOPTAN[1,4]

1. Center for Micro Electro Mechanical Systems (CMEMS), University of Minho (UMinho), 4800-058 Guimarães, Portugal;
2. MIT Portugal Program, School of Engineering, University of Minho, Guimarães, Portugal;
3. Centre for Rapid and Sustainable Product Development Polytechnic Institute of Leiria, Rua General Norton de Matos, Apartado 4133, Leiria, Portugal;
4. IBTN/Br – Brazilian Branch of the Institute of Biomaterials, Tribocorrosion and Nanomedicine, UNESP, Campus de Bauru, Av. Eng. Luiz Edmundo Carrijo Coube, 14-01, 17033-360, Bauru, SP, Brazil

摘　要：用激光选区熔化(SLM)制备 Ti6Al4V 多孔结构，通过粉末冶金法充填 β-TCP 或 PEEK，以期提高材料的骨传导性和耐磨性能。考虑到这些结构对种植体长期性能的重要性，对其腐蚀行为进行探讨。结果表明，与致密结构相比，开放孔洞的引入导致更高的电化学动力学。β-TCP 和 PEEK 充填导致空洞或金属基体与充填材料之间产生间隙，影响多孔结构的腐蚀行为。

关键词：Ti6Al4V 多孔结构；腐蚀；多材料设计；PEEK；β-TCP

(Edited by Xiang-qun LI)